PAPER • OPEN ACCESS

A multiscale wavelet algorithm for atom tracking in STM movies

To cite this article: P K Messer *et al* 2022 *New J. Phys.* **24** 033016

View the article online for updates and enhancements.

New Journal of Physics
The open access journal at the forefront of physics

PAPER

OPEN ACCESS

A multiscale wavelet algorithm for atom tracking in STM movies

P K Messer[1], A-K Henß[1] (iD), D C Lamb[1,2,*] (iD) and J Wintterlin[1,2,*] (iD)

[1] Department of Chemistry, Ludwig-Maximilians-Universität München, Butenandtstr. 5-13, 81377 Munich, Germany
[2] Center for NanoScience, Schellingstr. 4, 80799 Munich, Germany
[*] Authors to whom any correspondence should be addressed.

E-mail: d.lamb@lmu.de and wintterlin@cup.uni-muenchen.de

Abstract

High-speed scanning tunneling microscopy (STM) data have become available that provide movies of time-dependent surface processes. To track adsorbed atoms and molecules in such data automatic routines are required. We introduce a multiresolution wavelet particle detection algorithm for this purpose. To identify the particles, the images are decomposed by means of a discrete wavelet transform into wavelet planes of different resolutions. An 'à trous' low-pass filter is applied. The coefficients from the wavelet planes are filtered to remove noise. Wavelet planes with significant coefficients from the particles are multiplied, and the product is transformed into a binary particle mask. The precision of the method is tested with data sets of adsorbed CO molecules and O atoms on a Ru(0001) surface. The algorithm can safely detect and localize these particles with high precision, even in the presence of the enhanced noise characteristic for high-speed, constant-height STM data. By linking the particle positions, we obtain extended trajectories with a resolution of $\sim$0.5 Å or better allowing us to investigate the detailed motion of single atoms on a surface.

1. Introduction

There is an increasing number of scanning tunneling microscopy (STM) studies in which much higher recording speeds than in standard setups have been achieved. Based on several instrumental improvements and by operating the STM in the constant height mode, rates of up to 100 images per second have been reached [1–5]. This is a considerable advance with respect to the minutes timescale on which images are usually recorded by STM. Atomically resolved movies have become accessible that provide insight into the dynamics of surface processes. For example, experiments performed in electrolyte solutions, showed that the hopping rates of adsorbed particles on an electrode surface are strongly affected by the electrical potential [6, 7]. And recently, it was observed that adsorbed atoms on a catalyst surface move through a dense adsorption layer at a surprising speed that is almost as high as on an empty surface [8].

The analysis of such data, which may consist of several thousand frames, requires algorithms that can automatically detect the adsorbed atoms and molecules, localize their positions with a sufficient precision to attribute them to the lattice sites of the single-crystal surfaces, and track their paths in successive images. Because of the characteristics of high-speed STM data, this is not a trivial task:

- The tunneling current preamplifier has to have a much higher band width than preamplifiers used in the slow, constant current mode. This condition is necessarily connected with an enhanced noise of the current signal.

- Images containing the additional, STM-typical line noise that is mainly caused by uncontrolled changes of the tunneling tip structure during scanning can be manually sorted out from the small data sets obtained by slow STM. For extended movies this is no longer feasible.

- The pixel resolution in STM movie data is usually low. In the x direction, along the line scan direction, this results from the limited digital sampling rate. In the y direction, the pixel resolution is given by the number of scan lines. This number is limited because the minimal time for one scan line is limited by the mechanical resonances of the STM. Hence, when a high frame rate is intended, the number of scan lines has to be low.

- The images are usually distorted by the use of sinusoidal or other non-linear piezo driving voltages [1, 3, 5]. The linear, saw-tooth driving voltages used in ordinary slow, constant-current STM contain higher harmonics that lead to mechanical vibrations and thus make imaging at higher scan rates impossibile.

- Atomic steps or the tilted background from a not perfectly horizontal sample may be more prominent than the atomic or molecular features to be tracked. This is problematic when a single threshold is used to recognize the features to be tracked and exists in standard as well as in high-speed STM.

- Also not restricted to high-speed STM is the problem that adsorbed atoms and molecules usually do not display simple Gaussian shapes. Localization methods based on a Gaussian profile can therefore not be used in general [9, 10].

- Thermal drift and piezo creep make it difficult to allocate atomic positions with respect to a lattice.

An early idea for atom tracking by STM that avoided several of these problems was to dispense with scanning altogether and keep the tip horizontally positioned over an adsorbed atom by means of a feedback controller [11, 12]. When the atom moved, the tip followed the atom and thereby determined the trajectory of the atom. However, because images were no longer generated, the environment of the moving atom was not visible and effects of neighboring atoms on the trajectories could not be studied. In other publications that dealt with ordinary 2D image sets, applications of pattern recognition techniques have been mentioned, but not described in detail [13, 14]. One detailed publication describes a tracking routine based on intensity thresholding, i.e., a feature in an image was identified as an adsorbed atom when the tunneling current in several neighboring pixels was higher than a defined threshold [15]. This relatively simple method works well as long as the signal from the adsorbed atoms is sufficiently strong but molecules that only weakly influence the tunneling current are probably difficult to analyze. Another atomic tracking method used a convolution of the STM images with a target image of a model atom [16]. This fast-Fourier transform (FFT)-based procedure, performed by calculating the cross-correlation of an image with a target image, is used in standard image processing methods for locating objects. With STM data, this approach worked well but, to discriminate between atomic features and noise, it required iterative construction of the model atom. It is also not clear how well it would work with data containing a lower signal-to-noise ratio or low pixel resolution. However, cross-correlation-based methods have successfully been applied for high-speed atomic force microscopy (AFM) movies of protein diffusion [17–19]. Target images were constructed by averaging over several molecules from the molecular ensembles in the movie data.

Here, we describe a method for particle tracking in video-rate STM movies consisting of several hundred to several thousand images based on a wavelet approach. The algorithm detects particles of various shapes in an environment of high noise and localizes their positions on the underlying single crystal surface. The particle positions are then linked in consecutive frames to generate trajectories. In a previous study, we have applied the algorithm to video-rate STM movies in order to track diffusing O atoms on a CO-covered Ru(0001) surface [8]. Here, we present a detailed description of the method.

2. The tracking algorithm

Before beginning with the tracking analysis, the data need to be prepared for tracking by first correcting the recorded images for the above mentioned distortions from the non-linear driving voltages. In the present case, where sinusoidal voltages were used, the method described in reference [5] is applied. The STM-typical line noise could also be removed first, at least partially, by applying filter routines [8, 20]. However, as we are interested in investigating the performance of the algorithm in the presence of this type of noise, we did not prefilter the data. Furthermore, the data were exclusively recorded on atomically flat terraces so that steps do not interfere with the analysis. We expect that the algorithm still works reasonably well in the presence of steps but have so far not studied such data in detail. One could also first remove steps from the images, e.g., by applying the method described in reference [15]. For the experiments presented here, the background from a tilted sample was already corrected during recording of the raw data by adding a fraction of the x driving voltage to the voltage controlling the vertical (z) direction in such a way that the scan lines were exactly horizontal [5].

When performing a single particle tracking (SPT) analysis *ex post facto*, typically two steps are required. The first step is the identification and localization of the individual particles in all images. In the second

step, the positions of the individual particles between the different images are connected. To improve particle detection, we used a wavelet approach.

2.1. Wavelet decomposition

There are several ways of acquiring or enhancing objects in an image. A simple way to enhance the contrast of objects in a noisy environment is to convolute the image with a 2D Gaussian function. The Gaussian function averages pixels in a certain area, reducing the variance between neighboring pixels and resulting in a smoothed image. In this way, the Gaussian acts as a low-pass filter, eliminating high spatial frequencies in the image caused by noise. The width of the Gaussian filter determines up to which scale objects are smoothed out and thus removed from the image.

More generally, other filters are available. Here, we do not use Gaussian functions but wavelets (an English/French composite for 'small waves'). Wavelets, commonly designated by ψ, are certain oscillatory functions that display a few oscillations in a limited time or space interval and quickly decay outside this interval [21, 22]. The local frequency of the oscillations, which is linked to the width of the interval, defines the size of features in the image that are enhanced. In wavelet terminology, the frequency and the related interval are referred to as the scale of the wavelet. By convoluting a wavelet with a signal I

$$\psi * I = W, \tag{1}$$

where the asterisk, $*$, is used to signify the convolution, a wavelet transform, W, is generated that contains the coefficients of the wavelet. In the continuous wavelet transform, W is a continuous function of the scale. Because of the localized nature of wavelets, the maxima in W, which occur at a certain scale, are correlated with the positions of features of similar sizes in the signal. In contrast to a Fourier transformation, a wavelet transformation can therefore be used to analyze signals both in the frequency and time domain, and can be used to investigate heterogeneous, dynamic systems [23]. These properties have been used for the analysis of seismic signals [24–26], and also for detecting and localizing objects in spatial data, e.g., in astronomical images [27] and in fluorescence microscopy images of biological samples [28]. Wavelet-based methods are also widely applied for image denoising [29–31] and compression [32].

In a discrete wavelet transform (DWT), a signal is decomposed into a finite number of wavelet transforms [33, 34]. The DWT replaces the convolution with continuous wavelet functions by a series of filters, each stage consisting of a pair of high and low-pass filters. Mathematically, the application of the high-pass filter is a convolution of the signal with a high-pass filter function g. In the present case, where the signal is a 2D STM image, $A_0(x, y)$, application of the first high-pass filter:

$$g * A_0 = W_1, \tag{2}$$

gives a transform $W_1(x, y)$, the so-called wavelet plane of detail level 1. It contains the fine details of the image, i.e., features appearing at (spatial) frequencies between the filter frequency and the maximum frequency given by the pixels of the image. The high-pass filtering corresponds to a wavelet transformation across this frequency band.

Application of the low-pass filter is a convolution with a low-pass filter function h. Its convolution with A_0 gives a low-pass-filtered image $A_1(x, y)$, the first, so-called approximation:

$$h * A_0 = A_1. \tag{3}$$

The approximation A_1 is then treated by the second pair of high and low-pass filters at half of the cut-off frequency of the first filter stage:

$$g * A_1 = W_2, \tag{4}$$

$$h * A_1 = A_2. \tag{5}$$

The resulting wavelet plane $W_2(x, y)$ highlights features of larger size than in W_1 and the approximation $A_2(x, y)$ is a more strongly low-passed filtered image than A_1. Halving of the frequency is usually realized by dyadic downsampling of the image. This procedure is repeated recursively. After j recursion steps, a set of wavelet planes $\{W_1, \ldots, W_j\}$ has been generated, each of which shows objects of different sizes at a different resolution. One therefore speaks of a multiresolution decomposition [33]. [When the filter functions are correctly chosen, the DWT preserves all information in the image and, from the set of wavelet planes together with the last approximation, $\{W_1, \ldots, W_j, A_j\}$, one can reconstruct the original image A_0. We do not use this property in the present application, which aims at the identification of particles in the W_i planes.]

2.2. The 'à trous' wavelet transform

From the available DWT algorithms [22, 34, 35], we adopt the 'à trous' (with holes) wavelet transform, which has been shown to be suitable for fast and robust particle detection in 2D imaging data [27]. In contrast to standard methods, it provides an efficient downsampling of relevant frequencies in an image without decreasing the image size.

For the first low-pass filter, the row vector $h_1 = \left[\frac{1}{16}, \frac{1}{4}, \frac{3}{8}, \frac{1}{4}, \frac{1}{16}\right]$ is used [27]. For computational efficiency, this 1D filter is applied consecutively to the two dimensions of the images, i.e., first a row by row convolution is performed, and then a column by column convolution with the corresponding column vector $h_1{}^T$. The orange box in figure 1 (top panel) shows the full, 2D shape of this filter function. To avoid discontinuities at the edges, the images are first symmetrically mirrored at the borders. Application of the first filter h_1 to A_0:

$$h_1{}^T * (h_1 * A_0) = A_1, \tag{6}$$

where $h_1{}^T$ is the matrix transpose of h_1, gives the first approximation A_1 (figure 1, red box, top panel). Because the à trous filter preserves the image size, the first detail level W_1 can be obtained without explicit high-pass filtering, simply by taking the difference between the original image and the first approximation:

$$A_0 - A_1 = W_1, \tag{7}$$

(figure 1, blue box, top panel). In the next step, the low-pass filter is expanded by inserting a zero (for $j = 2$) or, in general, $2^{j-1} - 1$ zeros, between the entries in the filter h_j for each detail level $j \in \mathbb{N}$ (hence the name 'à trous') [27, 34]. Expanding the filter has the advantage over image downsampling that the pixel sizes of the approximations and detail levels are preserved. Pixel positions therefore remain constant and the wavelet transform is translationally invariant. Both features are crucial for localizing the positions of particles in addition to their mere detection. The detail levels are obtained recursively by applying the expanded low-pass filter to the previous approximation and taking the difference to the current approximation:

$$h_j{}^T * \left(h_j * A_{j-1}\right) = A_j, \tag{8}$$

$$A_{j-1} - A_j = W_j, \quad \forall j \in \mathbb{N}. \tag{9}$$

The procedure is illustrated in figure 1. The original STM image, A_0, shows ten oxygen atoms (bright spots) adsorbed on a Ru(0001) surface and forming a cluster with a local (2×2) structure. The image is a small section from a larger image (figure 3), and it shows the relatively high noise and low pixel resolution often characteristic for video STM data. Better data can be obtained but, for the present purpose, we intentionally chose an example with only moderate quality. Figure 1 shows how the approximations and detail levels (red and blue frames, respectively) develop as the size of the filter (orange frame) is increased from $j = 1$ to $j = 4$. The number of reasonable detail levels is determined by the finite size of the images. For the 200 pixel $\times$ 200 pixel images usually analyzed in this work, detail levels are calculated up to $j = 6$, for which the size of the filter (129 pixels) almost reaches the number of pixels in one dimension.

2.3. Particle detection

The elegance of the method is that the wavelet coefficients in each detail level W_j are correlated to the actual size of an object localized at a certain pixel position. In a noise-free environment, all coefficients at positions without a particle would remain zero as no frequency components would be present. In the presence of noise, there is an uncorrelated carpet of non-zero values especially, but not exclusively, in the detail levels containing high frequencies (e.g. W_1, figure 1, blue frame, top panel). As outlined in the introduction, the two major sources of noise are the tunneling current pre-amplifier and intermittent structure changes of the tip. For our data, we treat all noise as additive, uncorrelated white noise. Most of this additive noise can be filtered out by applying a threshold on the coefficients in the wavelet planes W_j based on their median absolute deviation (MAD) $\overline{\sigma}_j$ [28]:

$$W_j^{\text{thr}}(x, y) = \begin{cases} W_j(x, y) & W_j(x, y) \geqslant 2\overline{\sigma}_j \\ 0 & \text{otherwise.} \end{cases} \tag{10}$$

The result is shown in the green frame in figure 1. We use the MAD instead of the standard deviation because it is more robust against outliers. Note that the coefficients in a wavelet plane do not necessarily follow a single type of distribution. In contrast to previous approaches for astronomical and biological images [27, 28], we obtain good results with a less harsh threshold of $2\overline{\sigma}_j$ as we use an additional selection step discussed next.
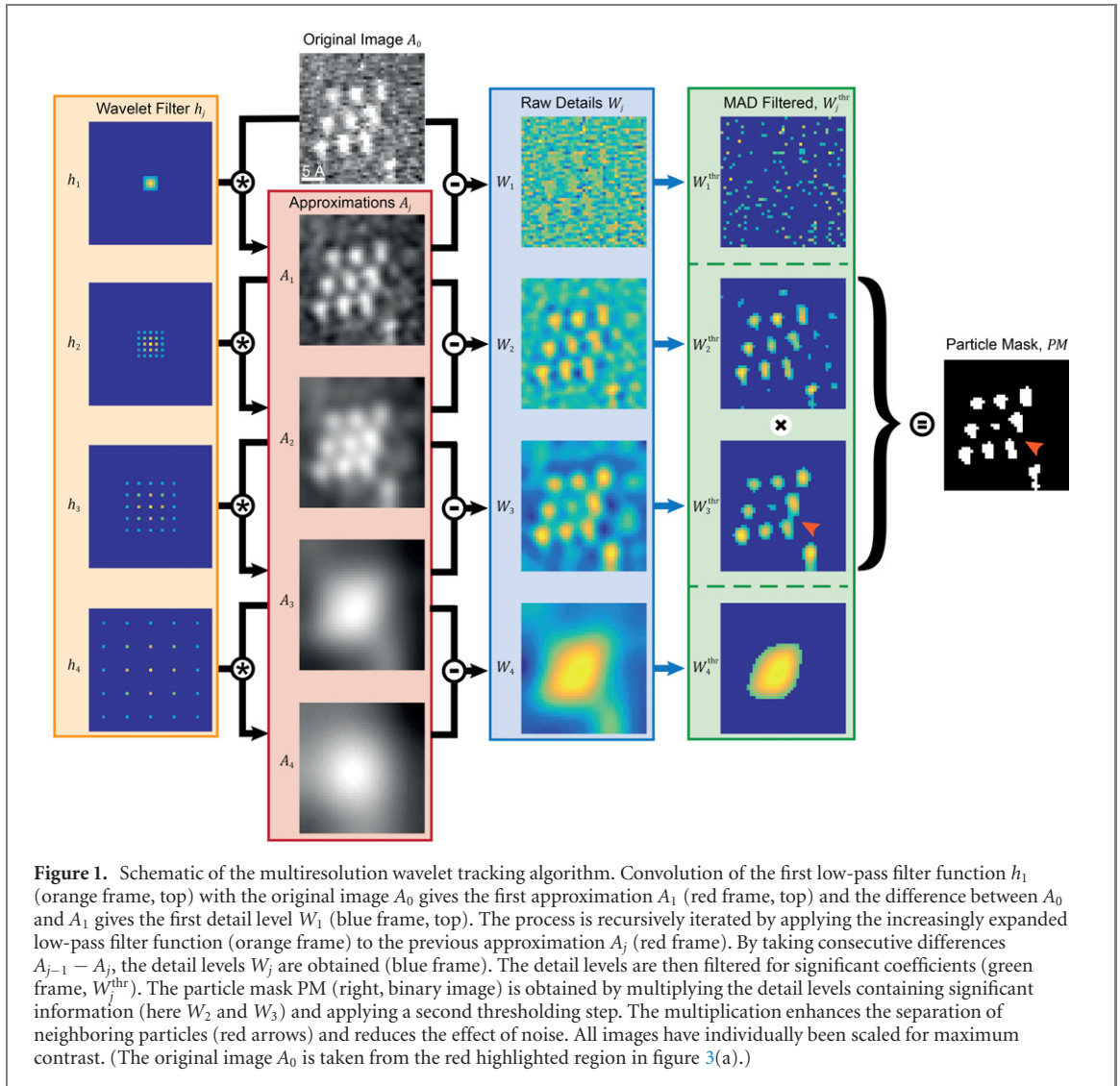
Figure 1. Schematic of the multiresolution wavelet tracking algorithm. Convolution of the first low-pass filter function h_1 (orange frame, top) with the original image A_0 gives the first approximation A_1 (red frame, top) and the difference between A_0 and A_1 gives the first detail level W_1 (blue frame, top). The process is recursively iterated by applying the increasingly expanded low-pass filter function (orange frame) to the previous approximation A_j (red frame). By taking consecutive differences $A_{j-1} - A_j$, the detail levels W_j are obtained (blue frame). The detail levels are then filtered for significant coefficients (green frame, W_j^{thr}). The particle mask PM (right, binary image) is obtained by multiplying the detail levels containing significant information (here W_2 and W_3) and applying a second thresholding step. The multiplication enhances the separation of neighboring particles (red arrows) and reduces the effect of noise. All images have individually been scaled for maximum contrast. (The original image A_0 is taken from the red highlighted region in figure 3(a).)

It has been suggested that the effects of the particles with respect to noise can be enhanced by calculating the product of the wavelet planes of all scales [28]. The idea is that particles should have non-zero coefficients on all detail levels, whereas this should not be the case for noise. The product should therefore only be significant at positions (x, y) where particles are localized. We use a modification of this approach because, in our case, the data may contain several types of particles, e.g. adsorbed O atoms and CO molecules [8], and these contribute differently to the different wavelet planes. Instead of multiplying all wavelet planes, we only utilize a subset $j = \{a, \dots, b\}$:

$$M_{a,b}\left(x, y\right) = \prod_{j=a}^{b} W_j^{\text{thr}}(x, y). \tag{11}$$

Selection of the detail levels to be included is done manually based on the visual appearance of the images and no *a priori* knowledge about the exact sizes of the particles is needed. This is normally done only once for a full data set with the same resolution and similar particle size. For the example in figure 1, it is obvious that the detail level W_1^{thr} only shows residual high-frequency noise not completely removed by the preceding thresholding. In detail levels W_2^{thr} and W_3^{thr}, the individual oxygen atoms are clearly visible. Toward higher j's, the detail levels no longer show individual atoms but an object the size of the entire cluster of atoms, as shown for W_4^{thr}. $M_{a,b}\left(x, y\right)$ is therefore only calculated with the two intermediate detail levels $j = \{2, 3\}$.

The resulting product is then transformed into a binary particle mask, PM. This is achieved by applying a threshold to $M_{a,b}$ such that all pixels with coefficients higher than the threshold are set to one and all

pixels with lower coefficients are set to zero.

$$\mathrm{PM}\left(x,y\right) = \begin{cases} 1 & M_{a,b}\left(x,y\right) \geqslant \text{threshold} \\ 0 & \text{otherwise.} \end{cases} \tag{12}$$

This second threshold is set manually in one or a few images of a movie and then applied to the entire movie for consistency. It is chosen such that it leads to sufficiently large coherent arrays of unity-valued pixels at the positions of the particles but, at the same time, avoids overlaps between neighboring particles. This is demonstrated for the binary particle mask for the subimage shown in figure 1. One can see that the product formation of W_2^{thr} and W_3^{thr} along with a careful setting of the threshold for the mask has created ten separate arrays for the ten atoms and has removed the critical intensity bridging between two neighboring O atoms in W_3^{thr} (red arrow).

2.4. Particle localization

After all particles in an image have been detected, their positions are determined. For this purpose, a morphological closing operation is first applied to the arrays of unity-valued pixels in the particle mask, PM. Single enclosed zero-valued pixels are set to unity by this operation. The resulting arrays represent the individual particles. Arrays with less than five pixels are discarded. This limit was found suitable for the data sets analyzed here and in reference [8]. In the case of considerably smaller or larger STM images, it may need to be adjusted. The exact particle positions are then determined by calculating the centers of mass of all pixels in the arrays belonging to the individual particles, resulting in a sub-pixel localization. There are more advanced techniques for particle localization utilized for fluorescence microscopy data [36, 37] but we find that these approaches work less well here due to the fact that they are based on having diffraction-limited particles and can therefore make use of the symmetry of the point-spread function. As visible in figure 1, the atomic features in STM data generally differ from that of an optical point-spread-function.

2.5. Particle linking

The next step in SPT is the linking of particles between neighboring frames of the movie, which allows trajectories of moving atoms or molecules to be extracted from STM movies. For the type of data analyzed in reference [8]—images containing a few, typically well-separated particles that usually move by short distances between two consecutive frames—this is relatively straightforward. Particles rarely come close to each other, and it is infrequent that a particle leaves or enters a frame or is intermittently lost because of an uncontrolled change in the tip structure during imaging.

For these conditions, a simple nearest-neighbor approach is appropriate and sufficient. To find the same particles in two successive frames, the distances between all particle positions in the current and the previous frame are calculated, resulting in a distance matrix of all possible connections. When the lateral distances have local minima in this matrix and do not exceed a defined tolerance radius, the positions of the particles in the current frame are linked to the positions in the former frame. (The tolerance radius depends on the data set; for the present data, values of around 7 Å are typically used.) When a second particle appears within the tolerance radius of a particle from the previous frame, the trajectory of this original particle is no longer unique and the trajectory is closed. When no particle is within the tolerance radius in the previous frame, the particle in the current frame is marked as new and a new trajectory is opened. When a particle in a former frame has disappeared in the current frame, its last position is kept for up to five frames and, when a particle is detected within the tolerance radius of this position within these five frames, its position is linked to the previous position. Otherwise, the trajectory is closed, and a particle appearing later at this position will be treated as a new particle. Such interrupted trajectories can result from a structural change to the tip. When this becomes obvious by a later manual examination of the data, two consecutive trajectories can be merged together into one coherent trajectory. At higher particle densities, linking becomes, of course, much more challenging and more advanced linking approaches can be applied [38].

2.6. Drift correction

In the last step, the trajectories are corrected for thermal drift and drift from piezo creep. Drift causes a slow shift of the imaged area with respect to the sample surface, adding a further translation vector to the actual movements of the particles. Signs for drift are unidirectional or even bent trajectories (when the drift changes with time). Therefore, drift has to be removed prior to a statistical analysis of the particle trajectories.

Drift can be removed by calculating the 2D cross-correlations between pairs of images, a method that has been successfully applied for AFM movies [39, 40]. In conventional, slow measurements, the drift would

usually be determined from the cross-correlation between consecutive images. The displacement at which the two images match best, given by the maximum in the correlation map, gives the drift vector in the x and y directions in units of integer pixels. In the present high-speed data, the drift between two consecutive images is always much lower than one pixel (typically of the order of 1/100 of a pixel), so that this method has to be modified. This is achieved by splitting the STM movies into several intervals and calculating the 2D cross-correlations between the first and last images of the intervals. The drift between two consecutive images within an interval is then evaluated by linearly interpolating between the first and last images in this interval. The lengths of the intervals are manually adjusted according to the respective form of the drift. Variable drift requires short intervals whereas a low constant drift can be more accurately corrected with longer intervals. The method works as long as there is one immobile atom or island in the interval, or when there are several atoms which only jump rarely.

3. Results and discussion

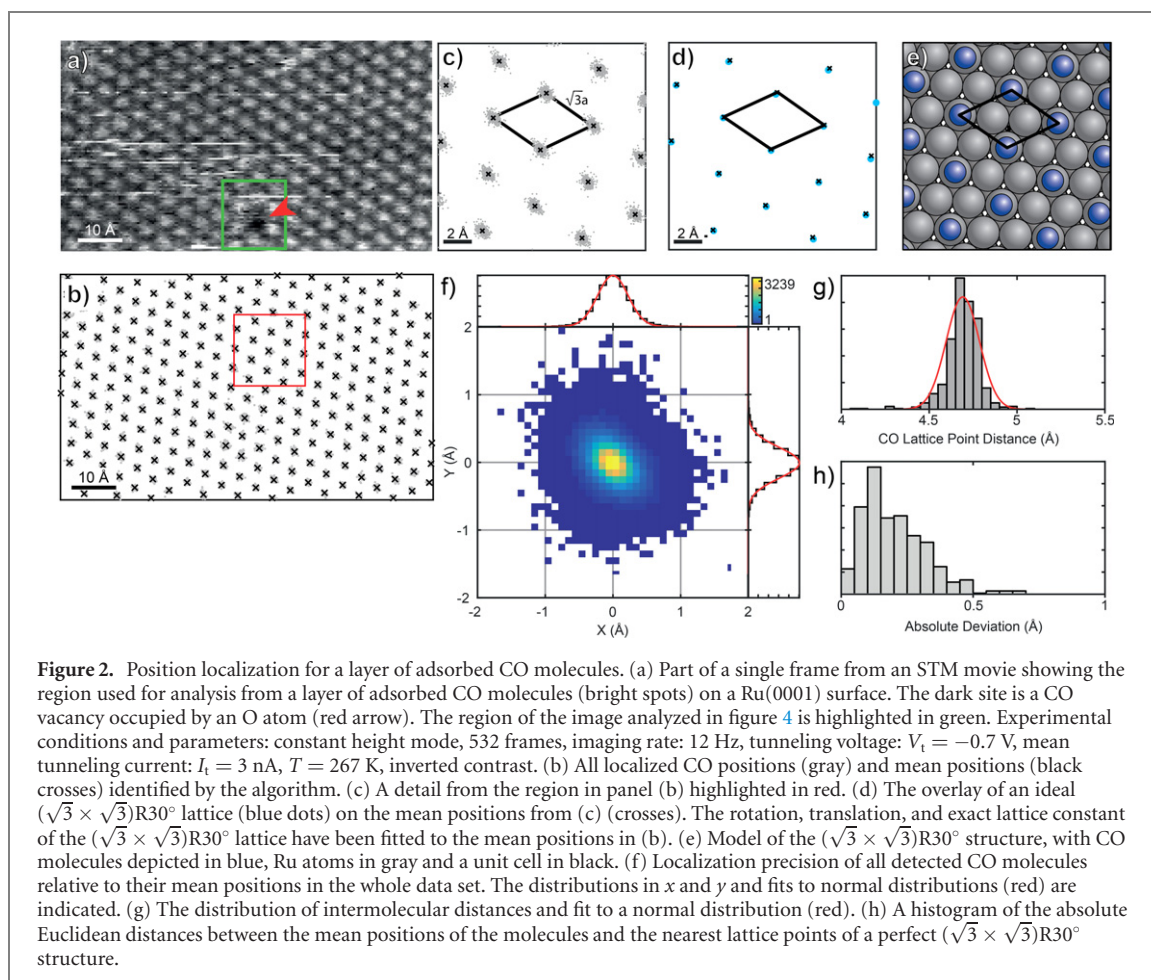### 3.1. Particle localization in a hexagonal layer of CO molecules on Ru(0001)

To test the performance of the algorithm, two data sets were analyzed, both of them from STM movies collected in the constant height mode at high speed. The first data set is from a Ru(0001) surface with a full layer of CO molecules and a low concentration of embedded O atoms. The second set is from the Ru(0001) surface with a low coverage of adsorbed O atoms. We first focus on particles that do not move, which enables us to characterize the localization precision of the algorithm. Figure 2(a) is a frame from the first data set, one of the movies analyzed in reference [8] but displayed here with inverted contrast. It shows a hexagonal pattern where the bright spots represent the CO molecules. The molecules form an ordered $(\sqrt{3} \times \sqrt{3})R30°$ structure (see the structure model in figure 2(e)) [41]. There is one dark site in the layer (figure 2(a), red arrow) where the CO layer has a vacancy which is occupied by a single O atom; these features are dynamic and will be analyzed further below. The ordered CO structure can, for the present purpose, be regarded as unchanging (in reality, there are fast fluctuations in the CO layer but these occur at a much higher rate than the time resolution of the STM, which shows time averaged positions of the CO molecules) [8, 42].

Figure 2(b) shows the center-of-mass positions (gray) of the CO molecules obtained by the wavelet localization algorithm from 532 successively recorded images. The averaged positions are marked by black crosses. The scatter of the positions is low and hardly visible on this scale. Figure 2(c) shows an expansion of the marked section (figure 2(b), red frame), where one can see the individual data points (gray areas around the crosses).

As a first check, we analyzed how well the average CO positions fall on a $(\sqrt{3} \times \sqrt{3})R30°$ lattice. For this purpose, the area of figure 2(c) was superimposed with a perfect hexagonal lattice (figure 2(d), blue dots), but leaving the exact lattice constant variable. This takes the fact into account that the pixel-to-Å calibration may vary somewhat between experiments. With these boundary conditions, the constructed lattice describes the averaged CO positions very well (figure 2(d), crosses). Of course, when the length calibration is performed in this way—using the crystallographic lattice constant of the $(\sqrt{3} \times \sqrt{3})R30°$ CO structure of 4.685 Å—the accuracy of the localization, i.e., the deviation between the average positions and the true lattice points cannot be quantified. However, the precision of the localization, i.e., the width of the distribution around the average positions, can be used as a quality measure. Figure 2(f) shows a 2D histogram of all determined CO positions with respect to their mean positions in the entire series and the cumulative distances in x and y direction. The precisions obtained from the FWHM of the normal distribution fits are 0.53 Å in x and 0.54 Å in y direction (table 1). The slightly elongated shape of the histogram results from residual drift that was not fully removed by the drift correction routine.

As another measure of the localization precision, we used the distribution of distances between adjacent CO molecules (figure 2(g)). The distribution is quite narrow and a fit to a normal distribution gives a FWHM of 0.22 Å. Assuming that the uncertainties in the positions of the individual particles are independent of each other, the distance distribution is a convolution of two normal distributions. Therefore, the FWHM has to be divided by $\sqrt{2}$, giving a value for the precision of 0.16 Å. As a third measure, we use the Euclidean distances between the mean CO positions and the lattice points of the $(\sqrt{3} \times \sqrt{3})R30°$ lattice constructed above (figure 2(h)). The mean deviation of 0.20 Å between the real and ideal positions is in good agreement with the precision determined from the intermolecular distances.

Hence, depending on which quality measure is used, the localization precision is between ca. 0.2 and 0.5 Å, with distances determined from neighboring molecules being approximately a factor 2 better. The precision is thus close to or even better than the pixel resolution of 0.4 Å per pixel in this particular experiment. The better precision determined from the molecular distances might be explained when some

Figure 2. Position localization for a layer of adsorbed CO molecules. (a) Part of a single frame from an STM movie showing the region used for analysis from a layer of adsorbed CO molecules (bright spots) on a Ru(0001) surface. The dark site is a CO vacancy occupied by an O atom (red arrow). The region of the image analyzed in figure 4 is highlighted in green. Experimental conditions and parameters: constant height mode, 532 frames, imaging rate: 12 Hz, tunneling voltage: $V_t = -0.7$ V, mean tunneling current: $I_t = 3$ nA, $T = 267$ K, inverted contrast. (b) All localized CO positions (gray) and mean positions (black crosses) identified by the algorithm. (c) A detail from the region in panel (b) highlighted in red. (d) The overlay of an ideal $(\sqrt{3} \times \sqrt{3})$R30° lattice (blue dots) on the mean positions from (c) (crosses). The rotation, translation, and exact lattice constant of the $(\sqrt{3} \times \sqrt{3})$R30° lattice have been fitted to the mean positions in (b). (e) Model of the $(\sqrt{3} \times \sqrt{3})$R30° structure, with CO molecules depicted in blue, Ru atoms in gray and a unit cell in black. (f) Localization precision of all detected CO molecules relative to their mean positions in the whole data set. The distributions in x and y and fits to normal distributions (red) are indicated. (g) The distribution of intermolecular distances and fit to a normal distribution (red). (h) A histogram of the absolute Euclidean distances between the mean positions of the molecules and the nearest lattice points of a perfect $(\sqrt{3} \times \sqrt{3})$R30° structure.

of the uncertainty in the particle positions was caused by variations of entire frames, e.g., by an imperfectly corrected drift or longer-lasting tip structure changes. In this case, the distances between the molecules within the individual frames would be less affected than the overall localizations over the full movie. However, even an overall precision of 0.5 Å is still a factor of 5 better than the lattice constant of Ru(0001) of 2.705 Å.

3.2. Particle localization at a low coverage of oxygen atoms on Ru(0001)

The same analysis was performed with the second data set, a movie of adsorbed O atoms (figure 3(a), bright spots) on an otherwise uncovered Ru(0001) surface. There are attractive interactions between the O atoms that, at the low coverage of this experiment, lead to small clusters with a local (2×2) structure. The O atoms appear roughly triangular, reflecting their threefold adsorption sites [43]. A structural model is shown in figure 3(b). The slight asymmetry of the triangles is an artifact from the tip shape.

To test the precision of the particle localization, a sequence of 1073 frames was analyzed. In a few frames in this series, which has been taken at 262 K, one of the O atoms jumped to a neighboring adsorption site. Because we are interested, at this point, in the positions of immobile atoms, these events were discarded. Figure 3(c) shows the resulting center of mass positions from the atoms in the cluster marked in figure 3(a). The scatter of the positions around the average positions is, again, quite low. This is also reflected by the 2D histogram of the positions of all O atoms in the area with respect to their mean positions in the series (figure 3(d)). Normal distributions fitted to the data along x and y give a FWHM of 0.62 Å and 0.63 Å, respectively, representing the localization precision for this example (table 1). In this case, the histogram is almost circular, indicating that the drift correction worked well. As in the CO case, the distribution of distances between the atoms was also evaluated, although here the result is less significant because of the low number of neighbors. A value of 0.25 Å was obtained for this second precision measure. Overall, the positions of the O atoms are localized with similar precision as in the case of the CO molecules.
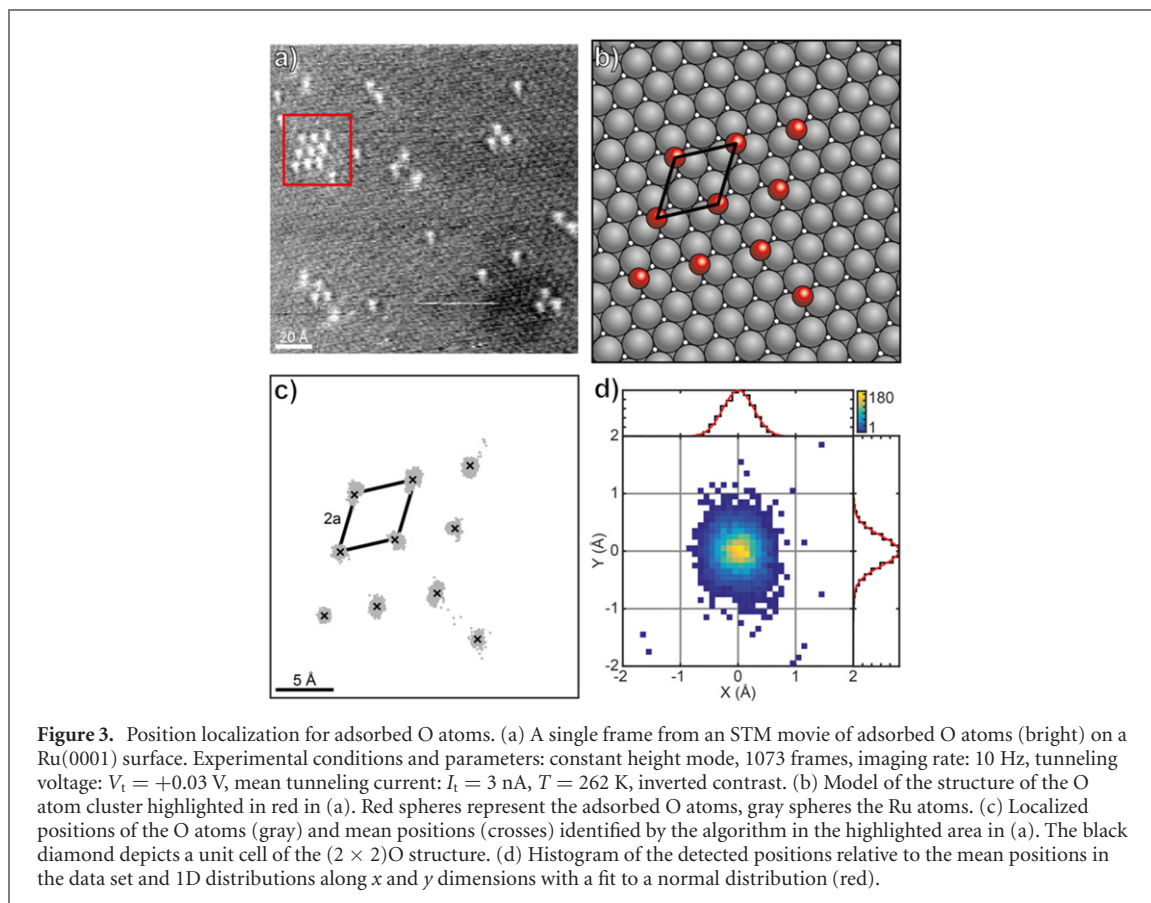
3.3. Limitations for the particle localization in the STM data

As outlined in the introduction, a localization algorithm applied to high-speed STM data has to deal with several specific problems. One is the enhanced noise. For comparison, we show an STM image of CO

Table 1. Data evaluation of the wavelet algorithm with respect to the localization precision and to the precision from interparticle distances.

Particle	Precision with respect to average positions			Precision from interparticle distances
	x	y		
CO	0.53 Å	0.54 Å	0.42 Å*	0.16 Å
O	0.62 Å	0.63 Å		0.25 Å

*FWHM perpendicular to the direction of drift.

Figure 3. Position localization for adsorbed O atoms. (a) A single frame from an STM movie of adsorbed O atoms (bright) on a Ru(0001) surface. Experimental conditions and parameters: constant height mode, 1073 frames, imaging rate: 10 Hz, tunneling voltage: $V_t = +0.03$ V, mean tunneling current: $I_t = 3$ nA, $T = 262$ K, inverted contrast. (b) Model of the structure of the O atom cluster highlighted in red in (a). Red spheres represent the adsorbed O atoms, gray spheres the Ru atoms. (c) Localized positions of the O atoms (gray) and mean positions (crosses) identified by the algorithm in the highlighted area in (a). The black diamond depicts a unit cell of the (2×2)O structure. (d) Histogram of the detected positions relative to the mean positions in the data set and 1D distributions along x and y dimensions with a fit to a normal distribution (red).

molecules on a Ru(0001) surface (similar to figure 2) recorded in the standard slow, constant current mode (supporting information (https://stacks.iop.org/NJP/24/033016/mmedia), figure S1). The noise level in the high-speed data is much higher, as expected. Nevertheless, from the two examples above, we show that the precision of the method is sufficient to localize the particles with a precision considerably better than the lattice constant of the Ru surface.

In addition to the average noise, we occasionally observe perturbations in single frames, mainly due to line artifacts from tip structure changes. These effects can be considerably stronger than the average noise and can be problematic for the tracking of moving particles. This is particularly true when the residence time of an atom at a given adsorption site is only one or a few frames before it moves to a neighboring site. We investigate how well our algorithm can deal with line artifacts. Three examples are shown in supporting information, figure S2, where line artifacts occur right at the position of a particle under study. With one exception, the wavelet algorithm was still able to localize the particles satisfactorily.

Another potential problem in high-speed STM imaging is the distortion from the non-linear driving voltage of the scanning piezo. In the present case where a sinusoidal voltage has been applied, this distortion was rectified in a relatively simple way by applying a recalibration function to the x axis [5]. Visually, the corrected images no longer appear distorted, as one can see, e.g., for the $(\sqrt{3} \times \sqrt{3})$R30° structure in figure 2(a). To investigate whether the localization precision is still affected despite the rectification process, the data points of figure 2(b) are divided into five parallel stripes along the y axis and the precisions were determined separately (supporting information, figure S3). No clear trend was detected. The precision at the outmost stripes, where one expects the strongest effect, is not significantly different from the middle positions.

Figure 4. Tracking of a moving oxygen atom in a CO layer on Ru(0001). (a) Model showing an O atom (red) in a vacancy of the layer of CO molecules (blue). The O atom occupies one of three possible threefold-coordinated sites with a Ru atom of the second layer underneath (hcp sites) (the dashed circles mark the two other, equivalent adsorption sites that can be occupied by the O atom). (b) An STM image showing the O atom (bright) and the neighboring CO molecules (dark). The image is a detail from one of the frames from the data set of figure 2 (highlighted in figure 2 in green); same tunneling parameters as in figure 2, but normal contrast. A mov movie of the series is available (supporting information, movie), in which the time-dependent position of the O atom is marked by a red dot. (c) Trajectory of the O atom in the movie of 532 frames; frame numbers are color-coded. Red circles mark the positions identified as outliers. The trajectory is corrected for the drift visible in the mov movie. (d) The same trajectory superimposed on the STM image, showing the correlation of the triangles in the trajectory with the three possible positions of the O atom in the CO vacancy. Experimental conditions and parameters: constant height mode, 532 frames, imaging rate: 12 Hz, tunneling voltage: $V_t = -0.7$ V, mean tunneling current: $I_t = 3$ nA, $T = 267$ K.

Regarding drift, the slight distortion of the histogram of figure 2(f) along the diagonal (which is the direction of the drift in this movie) from residual uncorrected drift has already been mentioned. When we take the FWHM of a cross section perpendicular to the drift vector instead of the cardinal directions, the precision improves from 0.53 and 0.54 Å to 0.42 Å. The non-perfectly compensated drift makes the precision worse by the order of 0.1 Å, whereas, in figure 3(d), drift artifacts are no longer measurable.

One could consider applying more elaborate methods for particle localization than using the simple center of mass. For example, one could average the particle masks in a movie to generate an overall molecular shape and then fit the individual molecules to the average shape. One could also first apply filters to the particle masks PM that correct for shape irregularities. For example, the pixel arrays of the particles could be smoothed by filling in or removing pixels at the borders, depending on the coordination numbers, to give more rounded forms. However, considering the overall precision of approximately 0.5 Å or better, we found it unnecessary to employ such filters.

3.4. Tracking of mobile oxygen atoms in the CO layer

The complete algorithm, consisting of the localization and the linking of the positions of the particles, was assessed by tracking O atoms embedded in a layer of CO molecules on Ru(0001) (figure 4(a)). Despite the dense CO layer, the O atoms are still mobile [8]. One of the embedded O atoms is visible in figure 2(a). Figure 4(b) shows an enlarged detail of this area with inverted contrast (i.e., the O atom is bright and the CO molecules are dark). The asymmetric position of the O atom with respect to the six surrounding CO molecules is clearly observable, which is explained by the different adsorption sites for the two species. The structure model in figure 4(a) illustrates the vacancy in the CO layer and the O atom that occupies one of three equivalent threefold absorption sites inside the vacancy.

Figure 4(c) shows the trajectory of the O atom obtained by the tracking algorithm from the analysis of 532 frames. The links between the positions of the O atom are color-coded with time. The shape of the trajectory is striking, exhibiting a row of connected triangles. This can be understood by the fact that the O atom is trapped for some time in the CO vacancy where it randomly jumps between three equivalent adsorption sites, leading to the triangles. Occasionally, there is a site exchange with neighboring CO molecules, after which the O atom is again trapped for a while within the new vacancy [8]. Figure 4(d)

illustrates the correlation between the positions of the O atom and the features imaged by the STM. A movie of the entire series is available (supporting information, movie).

As a measure of the quality of the tracking algorithm, we use the Jaccard similarity coefficient (JSC) [38]. The JSC is defined as the ratio of true positive detections to the sum of true and false positive and false negative detections. In the case shown, the tracking algorithm detects the atom in 529 out of 532 frames. Nine of the positions (figure 4(c), red dots) do not localize with the lattice sites. We treat them as outliers and count them as false positives. Assuming that the atom is present in every frame, the JSC is $520/532 = 0.98$ from a maximum of 1.

The JSC will be affected by the chosen threshold of W_j^{thr} and by the tolerance radius for the linking of particles in consecutive frames. In general, we choose relatively strict parameters, although the resulting trajectories are shorter because the lower number of true positives leads to more frequent interruptions. However, the fraction of false positives is also reduced, and this leads to a better quality of the statistical analysis of the trajectories.

3.5. Comparison with FFT-based methods

Wavelets are just one of several approaches that can be used to filter out features on particular length scales in an image. As mentioned in the introduction, mostly FFT-based methods have been used in previous STM and AFM work in which the images were convoluted with the image of a target atom or molecule [16–19]. These methods are straightforward but the construction of the target particle, which is usually performed by averaging over several particles, requires some effort. In the present wavelet-based method, no such input is required as the information about the particles is directly apparent in a small number of detail levels, e.g., W_2 and W_3 in figure 1. Objects of different dimensions can thus simply be sorted out. This direct access to the proper length scale is the strongest advantage of wavelet-based methods.

The systems investigated here, adsorbed O atoms and CO molecules on a metal surface, are relatively simple. For more complex objects that display a substructure in the images, FFT provides straightforward methods for identifying these objects whereas it may be more challenging for the wavelet approach. In a wavelet method, the substructure becomes visible in one or a few of the detail levels [23]. For particle localization in these cases, more elaborate techniques than the threshold procedure applied here may be needed. Moreover, wavelet analyses provide a range of flexibility as there are many functions that can be utilized as wavelets.

Another issue that arises when identifying non-symmetrical particles in an image is the orientation dependence. In the example investigated here (figure 4), the O/CO configuration has three different orientations that contribute with the same weight in the analysis. The O atom was correctly identified by the algorithm in all three orientations, as intended in this case. When determination of the orientation is required, both methods can successfully be applied. FFT-based methods can be performed with stepwise rotated target images. For wavelet methods, stretched or orientational wavelet functions have been applied [23, 44].

A critical property of particle localization methods is how well they can distinguish neighboring objects. As shown here for two neighboring O atoms (figure 1, W_3^{thr}), this worked well even in the high-noise environment of the given data set. FFT-based methods will presumably perform similarly well in this aspect. Ultimately, the approach that works best will depend on the quality of the data, the noise level, and on the type of noise.

4. Conclusions

We have developed a wavelet-based algorithm to track atoms and molecules in STM movies. The algorithm makes use of the unique property of wavelets to identify objects of a defined size and localize their positions in an environment of high noise. The algorithm has been tested with two data sets exhibiting the typical characteristics of high-speed, constant height STM data, namely high noise from the current preamplifier, line artifacts from occasional changes of tip structure, and relatively low pixel resolutions.

In the examples investigated, adsorbed CO molecules and O atoms on a Ru(0001) surface, the particles are detected with a probability close to unity. Depending on which quality measure is used, the localization precision is between a factor of 5 and 10 times better than the lattice constant of the ruthenium surface (2.705 Å). The particles can therefore be uniquely allocated to their adsorption sites. After proper removal of thermal drift, piezo creep, and the distortions from the non-linear driving voltages, particle linking leads to extended trajectories with significantly higher resolution than the lattice constant.

The algorithm does not contain any features specific to the physical examples investigated here. Hence, we believe that it is generally applicable to the analysis of data from high-speed STM, a technique that is being increasingly applied. The particle trajectories can be statistically analyzed, providing insights into the dynamics of atomic surface processes. Of course, the algorithm could equally well be applied to movie data from other scanning probe techniques such as AFM.

5. Materials and methods

5.1. Video-rate STM measurements

The STM movies were recorded with a home-built, high-speed variable temperature STM that has been described in detail before [5]. The measurements were performed in an ultra-high vacuum chamber at a base pressure of 1×10^{-10} mbar and at sample temperatures between 234 and 303 K. Imaging rates were typically 10 or 12 frames per sec (200×200 pixel images); rates of 50 frames per second have been achieved at lower pixel resolution. The tunneling parameters (voltages, currents) are given in the figure captions. For the negative tunneling voltages mostly applied in the experiments, the O atoms appear bright and the CO molecules dark in the constant height images. At positive tunneling voltages, the contrast is reversed. The algorithm works with bright particles, so that data sets recorded under conditions where the particles appear dark are first inverted.

5.2. Wavelet tracking software

The analysis software was written in MATLAB R2015b and is freely available at: https://gitlab.com/phme/wavelet-tracking.

5.3. LoG tracking software

To compare our tracking algorithm with another approach, we used the TrackMate plugin [45] for ImageJ. In TrackMate, a Laplacian-of-Gaussian (LoG) filter is used to locate the position of the particle. For the LoG filter, a Gaussian filter, G_σ, with a manually given radius, r, is first applied to the original image, I, and the second order spatial partial derivatives at each pixel are summed in the two dimensions and multiplied by $\sigma^2 = r^2/2$:

$$\mathrm{LoG}_\sigma = \sigma^2 \left(\frac{\partial^2}{\partial x^2} + \frac{\partial^2}{\partial y^2} \right) * G_\sigma * I. \tag{13}$$

A threshold was manually selected (given in supplementary information, figure S2) depending on the details of the image. The location of the particle is taken from the local maxima for values above the given threshold. In TrackMate, the particles can also be linked in different frames using a linear assignment problem algorithm. However, for comparison to our wavelet tracking algorithm, we were only interested in the LoG localization of the particle, which is shown in figure S2. The TrackMate software is available at: https://imagej.net/TrackMate.

Supplementary material

See supplementary material for signal-to-noise in constant current STM data, for the effect of line noise on the particle detection, and for the effects of the rectification of the sinusoidal scanning. See also for a movie of the diffusion of the O atom through the layer of CO molecules.

Data availability statement

The data that support the findings of this study are available upon reasonable request from the authors.

ORCID iDs

A-K Henß ⓘ https://orcid.org/0000-0001-7468-9654
D C Lamb ⓘ https://orcid.org/0000-0002-0232-1903
J Wintterlin ⓘ https://orcid.org/0000-0002-0636-7538

References

[1] Wintterlin J, Trost J, Renisch S, Schuster R, Zambelli T and Ertl G 1997 Real-time STM observations of atomic equilibrium fluctuations in an adsorbate system: O/Ru(0001) *Surf. Sci.* **394** 159–69

[2] Magnussen O, Zitzler L, Gleich B, Vogt M R and Behm R J 2001 *In situ* atomic-scale studies of the mechanisms and dynamics of metal dissolution by high-speed STM *Electrochim. Acta* **46** 3725–33

[3] Rost M J *et al* 2005 Scanning probe microscopes go video rate and beyond *Rev. Sci. Instrum.* **76** 053710

[4] Esch F, Dri C, Spessot A, Africh C, Cautero G, Giuressi D, Sergo R, Tommasini R and Comelli G 2011 The FAST module: an add-on unit for driving commercial scanning probe microscopes at video rate and beyond *Rev. Sci. Instrum.* **82** 053702

[5] Henß A K, Wiechers J, Schuster R, Platschkowski V and Wintterlin J 2020 A beetle-type, variable-temperature scanning tunneling microscope for video-rate imaging *Japan. J. Appl. Phys.* **59** SN1007

[6] Tansel T and Magnussen O M 2006 Video STM studies of adsorbate diffusion at electrochemical interfaces *Phys. Rev. Lett.* **96** 026101

[7] Rahn B, Wen R, Deuchler L, Stremme J, Franke A, Pehlke E and Magnussen O M 2018 Coadsorbate-Induced reversal of solid–liquid interface dynamics *Angew. Chem., Int. Ed.* **57** 6065–8

[8] Henß A-K, Sakong S, Messer P K, Wiechers J, Schuster R, Lamb D C, Groß A and Wintterlin J 2019 Density fluctuations as door-opener for diffusion on crowded surfaces *Science* **363** 715–8

[9] Bobroff N 1986 Position measurement with a resolution and noise-limited instrument *Rev. Sci. Instrum.* **57** 1152–7

[10] Thompson R E, Larson D R and Webb W W 2002 Precise nanometer localization analysis for individual fluorescent probes *Biophys. J.* **82** 2775–83

[11] Swartzentruber B S 1996 Direct measurement of surface diffusion using atom-tracking scanning tunneling microscopy *Phys. Rev. Lett.* **76** 459–62

[12] Grant M L, Swartzentruber B S, Bartelt N C and Hannon J B 2001 Diffusion kinetics in the Pd/Cu(001) surface alloy *Phys. Rev. Lett.* **86** 4588–91

[13] Pedersen M Ø, Österlund L, Mortensen J J, Mavrikakis M, Hansen L B, Stensgaard I, Lægsgaard E, Nørskov J K and Besenbacher F 2000 Diffusion of N adatoms on the Fe(100) surface *Phys. Rev. Lett.* **84** 4898–901

[14] Guézo S, Taranovskyy A, Matsushima H and Magnussen O M 2011 Surface dynamics of lead adsorbates at the Cu(100)−electrolyte interface *J. Phys. Chem* C **115** 19336–42

[15] Jak M J J, Konstapel C, van Kreuningen A, Verhoeven J, van Gastel R and Frenken J W M 2001 Automated detection of particles, clusters and islands in scanning probe microscopy images *Surf. Sci.* **494** 43–52

[16] Renisch S 1999 Zur Diffusion adsorbierter Teilchen auf Einkristalloberflächen: Dynamische Untersuchungen mit den Rastertunnelmikroskop *PhD Thesis* Fachbereich Chemie, Freie Universität Berlin

[17] Husain M, Boudier T, Paul-Gilloteaux P, Casuso I and Scheuring S 2012 Software for drift compensation, particle tracking and particle analysis of high-speed atomic force microscopy image series *J. Mol. Recognit.* **25** 292–8

[18] Ando T, Uchihashi T and Scheuring S 2014 Filming biomolecular processes by high-speed atomic force microscopy *Chem. Rev.* **114** 3120–88

[19] Munguira I, Casuso I, Takahashi H, Rico F, Miyagi A, Chami M and Scheuring S 2016 Glasslike membrane protein diffusion in a crowded membrane *ACS Nano* **10** 2584–90

[20] Anguiano E and Aguilar M 1999 A cross-measurement procedure (CMP) for near noise-free imaging in scanning microscopes *Ultramicroscopy* **76** 39–47

[21] Daubechies I 1992 *Ten Lectures on Wavelets* (Philadelphia, PA: SIAM)

[22] Mallat S 2009 *A Wavelet Tour of Signal Processing—the Sparse Way* (Amsterdam: Elsevier)

[23] Toplak T, Palmieri B, Juanes-García A, Vicente-Manzanares M, Grant M and Wiseman P W 2017 Wavelet imaging on multiple scales (WIMS) reveals focal adhesion distributions, dynamics and coupling between actomyosin bundle stability *PLoS One* **12** e0186058

[24] Goupillaud P, Grossmann A and Morlet J 1984 Cycle-octave and related transforms in seismic signal analysis *Geoexploration* **23** 85–102

[25] Anant K S and Dowla F U 1997 Wavelet transform methods for phase identification in three-component seismograms *Bull. Seismol. Soc. Am.* **87** 1598–612

[26] Lockwood O G and Kanamori H 2006 Wavelet analysis of the seismograms of the 2004 Sumatra−Andaman earthquake and its application to tsunami early warning *Geochem. Geophys. Geosyst.* **7** Q09013

[27] Starck J-L, Murtagii F and Bijaoui A 1995 Multiresolution support applied to image filtering and restoration *Graph. Models Image Process.* **57** 420–31

[28] Olivo-Marin J-C 2002 Extraction of spots in biological images using multiscale products *Pattern Recognit.* **35** 1989–96

[29] Yansun Xu Y, Weaver J B, Healy D M and Jian Lu L 1994 Wavelet transform domain filters: a spatially selective noise filtration technique *IEEE Trans. Image Process.* **3** 747–58

[30] Murtagh F and Starck J-L 2000 Image processing through multiscale analysis and measurement noise modeling *Stat. Comput.* **10** 95–103

[31] Münch B, Trtik P, Marone F and Stampanoni M 2009 Stripe and ring artifact removal with combined wavelet—Fourier filtering *Opt. Express* **17** 8567–91

[32] Christopoulos C, Skodras A and Ebrahimi T 2000 The JPEG2000 still image coding system: an overview *IEEE Trans. Consum. Electron.* **46** 1103–27

[33] Mallat S G 1989 A theory for multiresolution signal decomposition: the wavelet representation *IEEE Trans. Pattern Anal. Mach. Intell.* **11** 674–93

[34] Shensa M J 1992 The discrete wavelet transform: wedding the a trous and Mallat algorithms *IEEE Trans. Signal Process.* **40** 2464–82

[35] Daubechies I, Grossmann A and Meyer Y 1986 Painless nonorthogonal expansions *J. Math. Phys.* **27** 1271–83

[36] Parthasarathy R 2012 Rapid, accurate particle tracking by calculation of radial symmetry centers *Nat. Methods* **9** 724–6

[37] Martens K J A, Bader A N, Baas S, Rieger B and Hohlbein J 2018 Phasor based single-molecule localization microscopy in 3D (pSMLM-3D): an algorithm for MHz localization rates using standard CPUs *J. Chem. Phys.* **148** 123311

[38] Chenouard N *et al* 2014 Objective comparison of particle tracking methods *Nat. Methods* **11** 281–9

[39] van Noort S J T, van der Werf K O, de Grooth B G and Greve J 1999 High speed atomic force microscopy of biomolecules by image tracking *Biophys. J.* **77** 2295–303

[40] Marchesi A, Gao X, Adaixo R, Rheinberger J, Stahlberg H, Nimigean C and Scheuring S 2018 An iris diaphragm mechanism to gate a cyclic nucleotide-gated ion channel *Nat. Commun.* **9** 3978

[41] Thomas G E and Weinberg W H 1979 The vibrational spectrum and adsorption site of CO on the Ru(001) surface *J. Chem. Phys.* **70** 1437–9

[42] Sakong S, Henß A-K, Wintterlin J and Groß A 2020 Diffusion on a crowded surface: kMC simulations *J. Phys. Chem* C **124** 15216–24

[43] Lindroos M, Pfnür H, Held G and Menzel D 1989 Adsorbate induced reconstruction by strong chemisorption: Ru(001)p(2 × 2)-O *Surf. Sci.* **222** 451–63

[44] Bekkers E, Duits R, Berendschot T and ter Haar Romeny B 2014 A multi-orientation analysis approach to retinal vessel tracking *J. Math. Imaging Vis.* **49** 583–610

[45] Tinevez J-Y, Perry N, Schindelin J, Hoopes G M, Reynolds G D, Laplantine E, Bednarek S Y, Shorte S L and Eliceiri K W 2017 TrackMate: an open and extensible platform for single-particle tracking *Methods* **115** 80–90